Fluorescence profile of a nitrogen-vacancy center in a nanodiamond

Qiang Sun[*] and Shuo Li

Australian Research Council Centre of Excellence for Nanoscale BioPhotonics, School of Science,
RMIT University, Melbourne, VIC 3001, Australia

Taras Plakhotnik

School of Mathematics and Physics, The University of Queensland, QLD 4072, Australia

Andrew D. Greentree[†]

Australian Research Council Centre of Excellence for Nanoscale BioPhotonics, School of Science,
RMIT University, Melbourne, VIC 3001, Australia

Nanodiamonds containing luminescent point defects are widely explored for applications in quantum biosensing such as nanoscale magnetometry, thermometry, and electrometry. A key challenge in the development of such applications is the large variation in fluorescence properties observed between particles, even when obtained from the same batch or nominally identical fabrication processes. By theoretically modeling the emission of nitrogen-vacancy color centers in spherical nanoparticles, we are able to show that the fluorescence spectrum varies with the exact position of the emitter within the nanoparticle, with noticeable effects seen when the diamond radius, a, is larger than around 100 nm, and significantly modified fluorescence profiles found for larger particles when $a = 200$ and 300 nm, with negligible effects below $a = 100$ nm. These results show that the reproducible geometry of point defect position within a narrowly sized batch of diamond crystals is necessary for controlling the emission properties. Our results are useful for understanding the extent to which nanodiamonds can be optimized for biosensing applications.

I. INTRODUCTION

Understanding nanoscale effects is one of the most exciting scientific endeavors. It underpins very diverse research areas such as the mechanisms of life [1–5], quantum information [6–8], and fundamental phenomena in condensed-matter systems [9–11]. Research in these areas requires nanoscale quantum sensors, and one of the most mature room-temperature quantum nanoscale sensors is nanodiamond containing the negatively charged nitrogen-vacancy (NV) center [12–14]. Such doped nanodiamonds are a superb system for quantum sensing. They are highly biocompatible [15,16] and photostable [17,18], and therefore are ideal for minimally invasive biological experiments.

When using NV centers, readout is typically achieved via optically detected magnetic resonance, where the resonances in the interaction of the electronic spin of NV centers and a radio-frequency electromagnetic field are detected by measuring the photoluminescence intensity of the centers. In this way, NV centers have been used for nanoscale magnetometry [19,20], electrometry [21,22], thermometry [23,24], and pressure measurements [25]. Alternatively, accurate measurements of the photon luminescence spectrum (in

particular its zero-phonon line) allow for all optical measurements [26].

A drawback of fluorescent nanodiamonds, in comparison to quantum dots and organic molecules, is their intrinsic heterogeneity. Large variations in fluorescence intensities and lifetimes are observed between NV centers in similar nanodiamonds [27–30]. Understanding the origins of such variations and the ways of reducing the heterogeneity is important for developing a reliable technological platform.

Deliberate modification of the NV fluorescence spectrum can be achieved by quantum electrodynamics processes. When a quantum system is placed in a node of a resonance mode of an optical cavity, the emission of photons at the wavelength of the resonance increases. In such a case, the overall emission spectrum will be different from that in free space (that is in a bulk crystal). In principle, this enhancement can be very significant and the resonance can be fine tuned to enhance zero-phonon emission and suppress emission at other wavelengths by changing particle size [31], or locating nanodiamonds on a substrate [32,33] or in a microcavity [34–36]. Structural resonances, also called whispering-gallery modes, in a small regularly shaped particle such as a sphere are examples of such modes. A strong effect can be achieved if there is a control over the position of the center inside the particle and the size of the particle. These conditions are hard to satisfy for NV centers in diamond. In this paper, we will not specifically address the problem of the structural resonances

[*]qiang.sun@rmit.edu.au
[†]andrew.greentree@rmit.edu.au

TABLE I. Probabilities (relative intensity R) to emit photons and phonons of a NV center in bulk diamond as a function of the number of phonons at low temperature calculated in [37]. The zero-phonon line is indicated by ZPL, and the phononic sideband arises from the summation from 1 to 11 phonons.

No. of phonons	Wavelength λ (nm)	Emission probabilities (Relative intensity R)	Dipole moment strength (arb. u.) ($|p| = \lambda^2\sqrt{R}$)
0 (ZPL)	637	0.0270	66674.65
1	659	0.0951	133924.83
2	683	0.173	194028.02
3	708	0.209	229160.45
4	736	0.191	236740.36
5	765	0.140	218971.14
6	797	0.0856	185846.13
7	832	0.0441	145367.04
8	870	0.0211	109946.08
9	912	0.00931	80253.60
10	957	0.00343	53637.80
11	1008	0.000980	31807.83

and assume a random position of the center. The effect is also reduced because the size of the crystals considered is comparable to or smaller than the wavelength of emitted light. In this case, the quality factor of the resonances is quite small. However, the fluctuations of the spectra demonstrated here are direct consequences of weak coupling to broad structural resonances of the sphere.

We show and analyze statistically the NV fluorescence by modeling the emission of a point defect in spherical nanodiamonds as a function of nanodiamond size, the defect position within the crystal, and the orientation of NV relative to the plane of light collecting aperture. We treat the NV coupled to phonons of the crystal lattice as a set of electric dipoles with different oscillation frequencies and emission probabilities [37,38]. The electromagnetic fields within and outside the diamond are calculated using Mie theory [39–42] and validated numerically [43]. In our calculations, modification of the density of states close to the crystal surface [44] is not considered. Our results show that noticeable variations in the shapes of NV emission spectra are negligible when a, the radius of the particle, is below 100 nm but are significantly modified if $a \approx 200$ nm and larger. Although our systems are idealized for computational tractability, the results highlight the sensitivity of fluorescence to the precise location of the NV with diamond crystal, and are therefore important for understanding the experimentally observed variations in fluorescence.

II. MODEL

To investigate how the NV center location within a nanodiamond particle affects the far-field fluorescence, we consider a single NV in a spherical particle with a refractive index of $n_2 = 2.4$ in air with a refractive index of $n_1 = 1.0$. The broad NV emission spectrum is represented by emission by 12 point dipoles $\boldsymbol{p} \equiv \boldsymbol{p}_i$ ($i = 0, 1, 2, \ldots, 11$) corresponding to the NV emitting a single photon and multiple phonons. This gives rise to a broad emission spectrum with components at different wavelengths, as listed in Table I. We use the low-temperature emission probabilities from [37,38] as the relative

intensity, R, emitted from the NV center at different numbers of deexciting phonons, but we expect similar results for the room-temperature case. Since intensity R is proportional to the field power, it is then proportional to the square of the strength of the represented electric dipole for the NV center. To match the dimension, we have $(c|\boldsymbol{p}|^2)/(4\pi\epsilon_0\epsilon_r\lambda^4) \sim R$ where c is the speed of light, ϵ_0 is the vacuum permittivity, ϵ_r is the relative permittivity, and λ is the wavelength of emission light. Since c, ϵ_0, and ϵ_r are constant in a homogeneous diamond, for simplicity, we set $|\boldsymbol{p}|^2 = \lambda^4 R$. In Figs. 2(c) and 2(d), the square symbols display the relative intensity R at the corresponding wavelengths.

To monitor the emission, we model a detector with circular entrance aperture (NA=0.9). The axis of the point dipole is assumed either parallel or perpendicular to the plane of the aperture, as sketched in Fig. 1. In a homogeneous medium, the intensity of each wavelength would be proportional to the photon emission probability in the actual spectrum at the same wavelength, which in turn is derived from the emission probabilities. However, the electromagnetic fields transmitted to the surrounding medium (air in this paper) are modified due to the boundary conditions on the surface of the particle and can be obtained by solving Maxwell's equations which are solved using the Mie theory (see Appendices A and B). After obtaining the electromagnetic fields, we can calculate the observed far-field intensity for each dipole as measured through the aperture located either at the top view position or the side view position. This is done by integrating the time-averaged Poynting vector over the corresponding aperture area:

$$I_{\mathrm{nd}}(\lambda_i) = \int_{S_{\mathrm{obj}}} \frac{1}{2}[\boldsymbol{E}^1 \times (\boldsymbol{H}^1)^*]_\perp \, dS \qquad (1)$$

with $i = 0, 1, 2, \ldots, 11$. The above formulations give the photon count rates relative to the intensities of a NV center in bulk diamond listed in Table I in which λ_i is the wavelength of the corresponding dipole, the superscript asterisk indicates the complex conjugate, and $\perp$ in the subscript shows the component of the vector product perpendicular to the plane of the aperture.
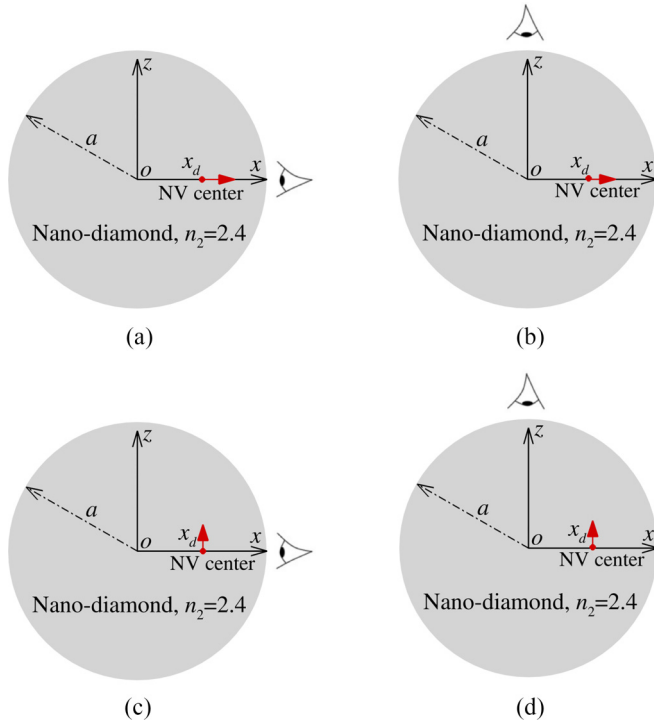
FIG. 1. Four cases under consideration for the photon collections by a circular optical objective with NA=0.9 emitted from a single NV center, which is represented by an electric dipole with moment $\boldsymbol{p}$, implemented in a spherical nanodiamond when the NV center is located at different position along the x axis: (a) case A, $\boldsymbol{p} = (p, 0, 0)$ and side view; (b) case B, $\boldsymbol{p} = (p, 0, 0)$ and top view; (c) case C, $\boldsymbol{p} = (0, 0, p)$ and side view; and (d) case D, $\boldsymbol{p} = (0, 0, p)$ and side view.

We also calculated

$$I_{\text{nd}}^n(\lambda_i) = \frac{I(\lambda_i)}{\sum_{i=0}^{11} I(\lambda_i)} \qquad (2)$$

for the normalized spectra which emphasize changes in the shape of the spectra rather than emission strength of the entire spectral band.
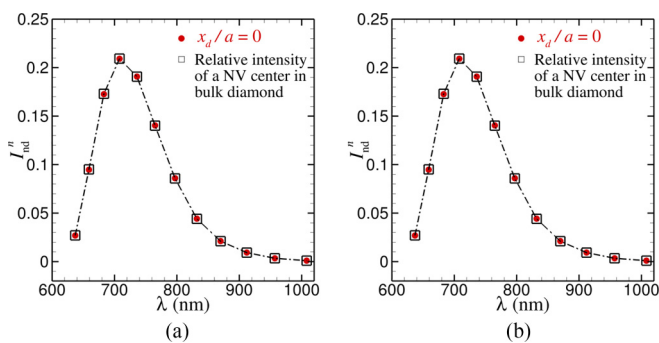

FIG. 2. The normalized photon counts at $x_d/a = 0$ for (a) case A and (b) case D, which almost fully represent the relative intensities of a NV center in bulk diamond at the low-temperature condition listed in Table I.

III. RESULTS

To demonstrate how the position of the NV center in a spherical nanodiamond can affect the photon collections at the far field, we locate the NV center at varying positions along the x axis, $\boldsymbol{x}_d = (x_d, 0, 0)$ and $|x_d| = d$. The equivalent electric dipole moment, $\boldsymbol{p}$, can be either along x axis or z axis. Together with two observation spots, the top view and the side view, as shown in Fig. 1, we studied four cases: (i) case A, $\boldsymbol{p} = (p, 0, 0)$ and side view; (ii) case B, $\boldsymbol{p} = (p, 0, 0)$ and top view; (iii) case C, $\boldsymbol{p} = (0, 0, p)$ and side view; and (iv) case D, $\boldsymbol{p} = (0, 0, p)$ and side view. Corresponding to cases A–D, the animations of the overall and normalized photon counts for $a = 10$ to 300 nm when the NV center is located from the left to the right of the particle are presented; see Supplemental Material [45] for overall and normalized photon counts. Also, the detailed analysis for different size of particles is demonstrated below.

We start with the case of a small nanodiamond with a radius of $a = 10$ nm. When the particle size is small compared to the wavelength of the emitted light from the NV center, the relative position of the NV center to the surface of the diamond particle has insignificant effects on the photon collection by the optical objective (the pin hole) [46], as displayed in Fig. 2. One main reason for that is that as the particle size is small, the field inside the particle is dominated by the near field of the represented electric dipole, and the particle surface is polarized nearly uniformly by such near-field profile of the electric dipole. As such, the relative position of the NV center has negligible effects on photon collection by the optical objective. In Fig. 2, we only show the overall and normalized electromagnetic intensity profiles for case A and case D as a function of the number of deexciting phonons, which almost fully represent the relative intensities of a NV center in bulk diamond at the low-temperature condition listed in Table I. For case B and case C, the profiles are the same as what are presented in Fig. 2, and hence are not repeated here.

When the radius of the diamond particle is 100 nm, the effects on the photon counts emitted from the NV center due to its location relative to the nanodiamond surface start to present. As the particle size increases, the near-field phenomenon from the electric dipole becomes a local effect, and the coupling between the radiation wave from the dipole and particle cavity starts to merge. For example, when the equivalent electric dipole moment direction is along the x axis, the overall electromagnetic-field intensity collected by the objective from side (case A) and top (case B) view is stronger when the dipole is located in the center of the diamond particle relative to when it is close to the diamond surface, as shown in Figs. 3(a) and 3(b). However, if the dipole moment direction is along the z axis, the overall electromagnetic-field intensity is stronger when the dipole is close to the diamond particle surface on the left for the side view, as shown in Fig. 3(c). With the top view for z-oriented NV center, the overall electromagnetic-field intensity profile is symmetric with respect to the center of the diamond center. The emission is weaker when the dipole is near the center of the particle relative to when it is close to the particle surface, as displayed in Fig. 3(d).

When the radius of the diamond particle is 200 nm, the subtle effects that were predicted for the 100-nm particles
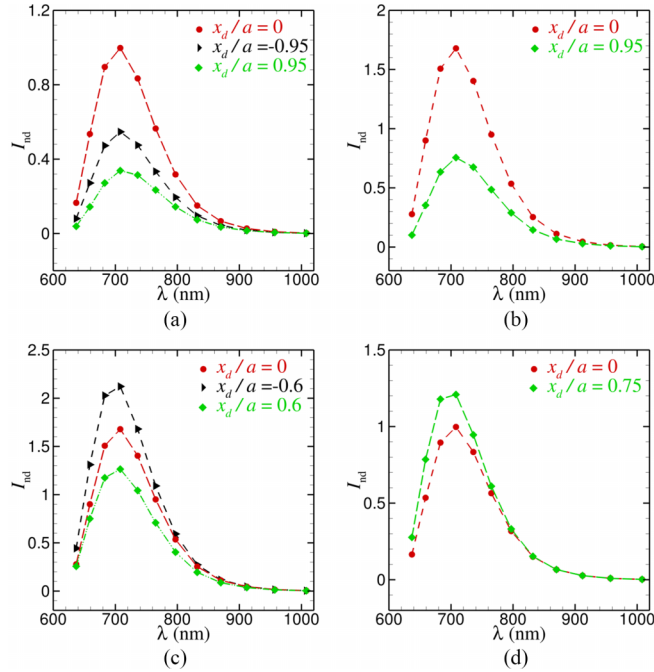
FIG. 3. The overall photon counts emitted from a NV center embedded in a nanodiamond with radius of $a = 100$ nm at selected NV center locations for (a) case A, (b) case B, (c) case C, and (d) case D. For the x-oriented dipole [(a) side view and (b) top view] the emission is higher when $x_d/a \approx 0$. For the z-oriented dipole, the emission is higher when the dipole is close to the diamond particle surface on the left for the side view (case C) while for the top view (case D), the emission is weaker when $x_d/a \approx 0$.
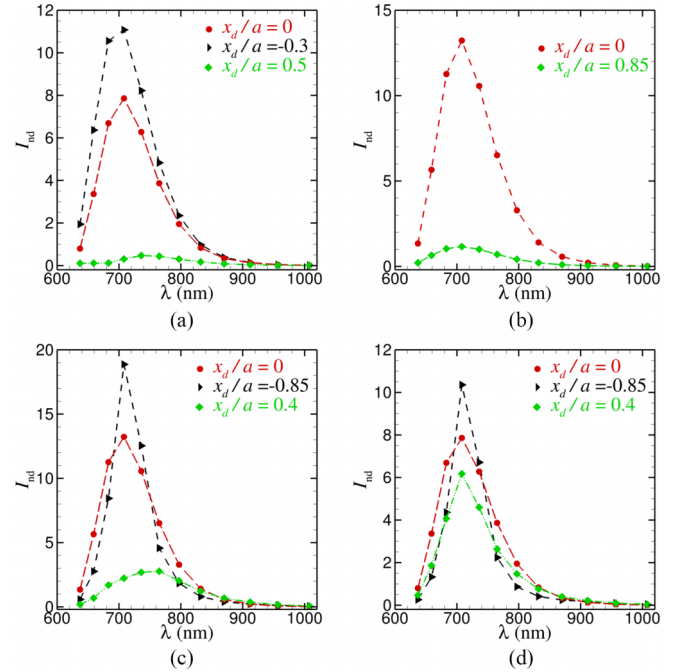

FIG. 4. The overall photon counts emitted from a NV center embedded in a nanodiamond with radius of $a = 200$ nm at selected NV color center locations for (a) case A, (b) case B, (c) case C, and (d) case D. From the side view (case A and C), the emission is stronger as $x_d/a < 0$ with both x- and z-oriented dipoles. From the top view, the emission is much enhanced when $x_d/a \approx 0$ for the x-oriented dipole (case B).

become far more pronounced. Large changes in both the overall and relative (normalized) spectra are observed. The spectra for the overall electromagnetic-field intensity for the four cases are shown in Fig. 4. If the equivalent electric dipole moment direction is along the x axis, the overall electromagnetic-field intensities collected from both the top and side views indicate that, when the NV center is deep in the nanodiamond particle, the fluorescence signals are much stronger than those when it is close to the particle surface, as shown in Figs. 4(a) and 4(b). Unlike the symmetric fluorescence profile from the top view, the nanodiamond is much brighter when the NV center locates in the left part of the particle ($x_d/a < 0$) from the comparison between $x_d/a = -0.3$ and 0.5 in Fig. 4(a), whereas if the dipole moment direction is in the z direction, for example, case C and D in Figs. 4(c) and 4(d), emission signals from the NV center are significant when it is either close to the particle surface or near the center of the diamond particle.

The normalized electromagnetic-field intensity profiles of a single NV center implemented in a nanodiamond with radius of 200 nm are shown in Fig. 5. For case A when the dipole moment is along the x axis and the photon collection is along the side view, the normalized electromagnetic-field intensity almost represents the relative intensities of a NV center in bulk diamond when the NV center is located in the left part of the nanodiamond particle ($x_d/a < 0$). Nevertheless, if the NV center is placed to the right part in the nanodiamond when $x_d/a > 0$, compared to the relative intensities of a NV center
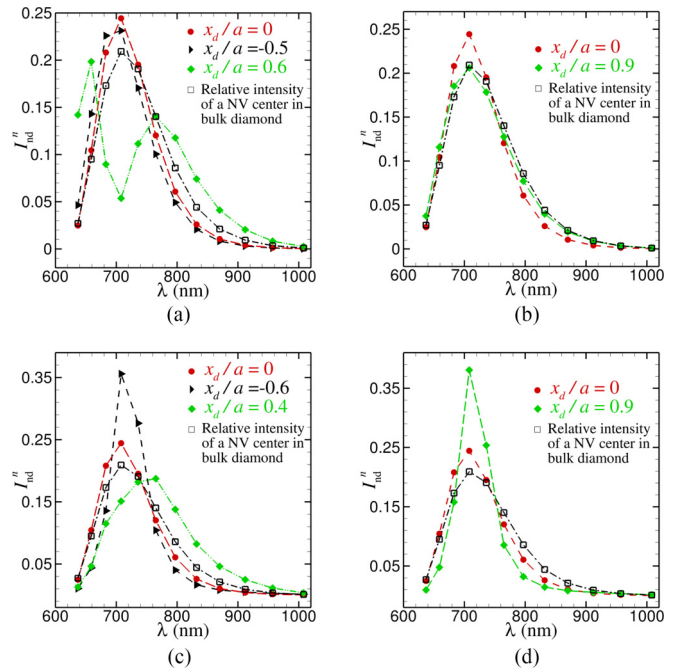

FIG. 5. The normalized photon counts emitted from a NV center embedded in a nanodiamond with radius of $a = 200$ nm at selected NV color center location for (a) case A, (b) case B, (c) case C, and (d) case D. For the x-oriented dipole from the side view (case A), when $x_d/a = 0.6$, the original emission peak at 709 nm disappears while two peaks appear at 659 and 765 nm.

in bulk diamond, dominant wavelength of the normalized electromagnetic-field intensity collected from the side view first changes from $\lambda = 708$ to 736 nm at around $x_d/a = 0.5$ and then changes again to $\lambda = 659$ nm at around $x_d/a = 0.6$, as shown in Fig. 5(a). Also, at $x_d/a = 0.6$, there is a second peak of the normalized electromagnetic-field intensity at $\lambda = 765$ nm, while the signal at 708 nm is significantly reduced. Regarding the top view as presented in Fig. 5(b) for case B, the normalized electromagnetic-field intensity profile is similar to that of a NV center in bulk diamond when the NV center is located from side to side in the particle. If the dipole moment direction is z oriented, both the side and top views show that the emission signal is enhanced significantly when the NV center is close to the surface of the particle ($|x_d|/a > 0.5$) for the wavelength at $\lambda = 708$ nm, as shown in Figs. 5(c) and 5(d). When the z-oriented NV center is deep in the particle, from the side view, the dominant number of deexciting phonons changes from 3 ($\lambda = 708$ nm) to 5 ($\lambda = 765$ nm) around $x_d/a = 0.4$, as shown in Fig. 5(c).

As the diamond radius increases to 300 nm, the spectra become richer. This is because there are numerous opportunities for resonances over the various wavelengths. For a diamond particle with radius of 300 nm, if the equivalent electric dipole moment direction is in the x direction, the overall electromagnetic-field intensity at $\lambda = 708$ nm is much stronger when the NV center is around $x_d/a = -0.5$ in the particle from the side view, as shown in Fig. 6(a) for case A. From the top view, the symmetric profile of the field intensity with respect to the particle center is obtained when the NV center is located from one side to the other of the particle, and the strongest fluorescence signal happens at $|x_d|/a = 0.55$ for $\lambda = 708$ nm, as shown in Fig. 6(b) for case B. When the dipole moment direction is pointing along the z axis, the highest fluorescence signal happens at $x_d/a = -0.4$ for $\lambda = 708$ nm from the side view, as shown in Fig. 6(c), while from the top view, the electromagnetic-field intensity profile is symmetric to the particle center and the strongest appears at around $|x_d|/a = 0.4$ for $\lambda = 708$ and 736 nm. Also, for these two cases, when $x_d/a = -0.75$ from the side view and $|x_d|/a = 0.85$ from the top view, there are two peaks of the fluorescence signals at $\lambda = 683$ and 832 nm while the original peak signal at $\lambda = 708$ nm for a NV center in bulk diamond is significantly reduced.

On the normalized fluorescence signals when a NV center is located at different position in a diamond particle with radius of 300 nm, for case A and B when the electric dipole moment direction is along the x axis, the dominant emission fluorescence is the same as a NV center in bulk diamond at $\lambda = 708$ nm when the NV center locates close to the surface of the diamond particle, as shown in Figs. 7(a) and 7(b). When the NV center locates at $x_d/a = 0.3$, the dominant emission wavelength changes to $\lambda = 736$ nm, as shown in Fig. 7(a). For case C and D as the dipole moment direction is in the z direction, when the position of the NV center is close to the surface of the diamond particle, the strongest emission happens at $\lambda = 683$ nm relative to a NV center in bulk diamond at $\lambda = 708$ nm, as shown in Figs. 7(c) and 7(d). If the NV center location locates deeper in the diamond particle at around $x_d/a = 0.45$, the dominant emission is changed to $\lambda = 736$ nm. Also, when $x_d/a = -0.75$ from the side view and at
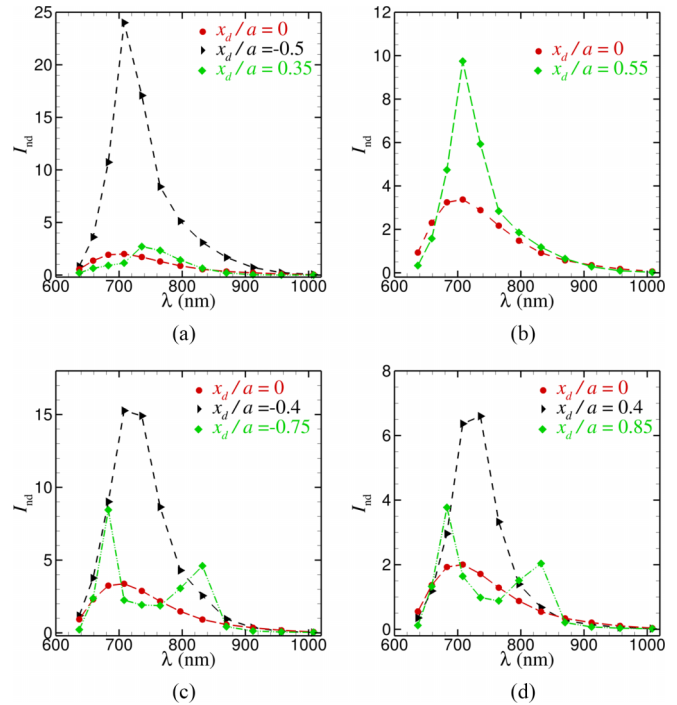

FIG. 6. The overall photon counts emitted from a NV center embedded in a nanodiamond with radius of $a = 300$ nm at selected NV color center locations for (a) case A, (b) case B, (c) case C, and (d) case D. For the x-oriented dipole, the emission is strongly enhanced when $x_d/a = -0.5$ from the side view (case A) and when $x_d/a = 0.55$ from the top view (case B). For the z-oriented dipole, the emission is highly enhanced when $x_d/a = -0.4$ from the side view (case C) and when $x_d/a = 0.4$ from the top view (case D). Also, the emission spectrum profiles are changed significantly when $x_d/a = -0.75$ from the side view and when $x_d/a = 0.85$ from the top view.

$|x_d|/a = 0.8$ from the top view for a z-oriented NV center, there are the two peaks of the normalized fluorescence signals at $\lambda = 683$ and 832 nm while the original peak signal at $\lambda = 708$ nm for a NV center in bulk diamond is significantly reduced.

When comparing the fluorescence profiles from a 300-nm diamond to those from the smaller diamonds, the emissions from longer wavelengths are enhanced in the 300-nm case. This is because the particle size at radius of 300 nm is comparable to the longer wavelengths when the high refractive index of diamond is taken into consideration, which leads to the enhanced cavity effects of the diamond particle for the emission at the higher-order lines [47].

IV. DISCUSSION

There are basically two effects on the emission spectra. One of them is the change of the integrated intensity, represented in Eq. (1), and the other is the change of the normalized spectra, represented in Eq. (2). Both effects depend on the position of the NV center within the crystal defined by x_d, on the orientation of its transition dipole moment, and on the crystal particle size a. Qualitatively, the variation of the overall intensity is negligible if $2\pi a\lambda \ll 1$ and the variation of
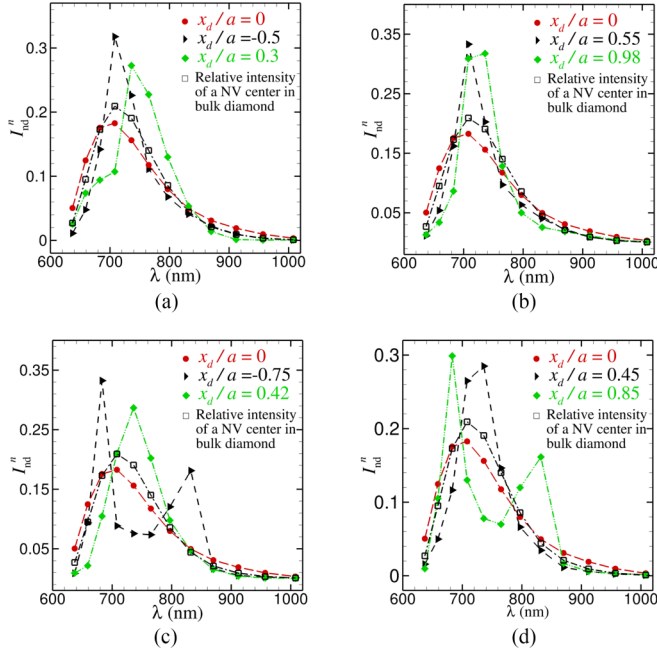
FIG. 7. The normalized photon counts emitted from a NV center embedded in a nanodiamond with radius of $a = 300$ nm at selected NV color center locations for (a) case A, (b) case B, (c) case C, and (d) case D. For the z-oriented dipole, the emission spectrum profiles are changed significantly relative to that of a NV center in a bulk diamond, for example when $x_d/a = -0.75$ from the side view (case C) and when $x_d/a = 0.85$ from the top view (case D).
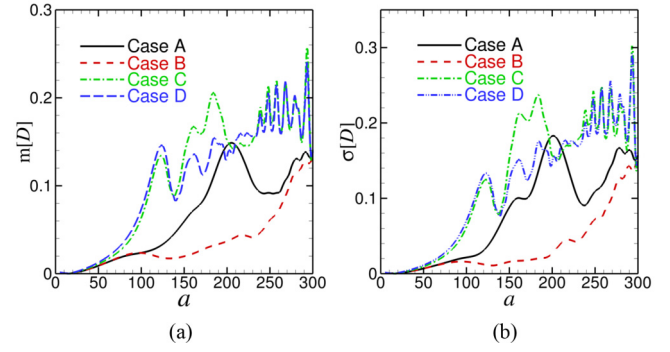

FIG. 8. Comparisons of the normalized emission spectra of a NV center in diamond particles to that in a bulk diamond: (a) the mean value and (b) the standard derivation of D defined in Eq. (3). As the diamond particle size increases, the overall trend of the mean value of D grows indicating that the normalized emission spectra of a NV center are more likely different in larger particles than smaller ones relative to the emission spectrum of a NV center in bulk.

the normalized spectra is negligible if $2\pi a\delta\lambda/\lambda^2 \ll 1$ where $\delta\lambda$ is the width of the luminescence spectrum of the center. For NV centers, the value $\delta\lambda/\lambda \approx 1/7$ and therefore the change in the normalized spectra are observed for significantly larger crystals.

It would be worth monitoring how the normalized emission spectra of a NV center in a diamond particle differ from those in a bulk diamond crystal. To characterize the difference, we calculate a value D defined as follows:

$$D(x_d, a) \equiv \sum_{i=0}^{11} \left| I_{nd}^n(\lambda_i, x_d, a) - I_{bulk}^n(\lambda_i) \right|, \quad (3)$$

in which $I_{nd}^n(\lambda_i, x_d)$ is defined in Eq. (2), and the values of $I_{bulk}^n(\lambda_i)$ are the relative intensity R listed in Table I. In the simulation, we assume that no NV centers are found within 2-nm distance from the surface of the particle [48] and the concentration of the centers is uniform in the remaining volume (that is, the probability of a particular value of r_d is proportional to r_d^2). For each particle with radius of a, we compute the mean value and the standard derivation of D using a random set of x_d to characterize how different the normalized emission spectrum is from that of a bulk diamond.

As shown in Fig. 8, the mean value of D starts to deviate from zero at x_d of about 50 nm. The relative deviation reaches 0.15 at 100 nm and oscillates significantly along with particle size for cases C and D (the dipole moment is perpendicular to the radial line of the sphere). In case B the mean relative deviation is below 0.05 up to 250 nm. The geometry of case B generates spectra which are least sensitive to the size of the

crystal and the position of the center. The standard derivation of D correlates to and has a similar trend as its mean value. In practice, the photoluminescence of the NV centers is associated with two orthogonal dipoles arranged in a plane perpendicular to the NV defect symmetry axis. This means that the cases A–C and B–D cannot be completely separated in an experiment. By reducing the numerical aperture of the detector, we can reduce the contribution of case A and D. Photoexcitation through the same optics also favors case B and C because the excitation beam is polarized in a transverse direction.

V. CONCLUSION

We performed theoretical modeling of the fluorescence profiles of a NV color center in a spherical nanodiamond, exploring the effects of the center location, orientation of its transition dipole moment, and nanodiamond size on the emission probabilities of NV center together. Changes in the emission probabilities lead to variations in the expected fluorescence profile. Our calculations indicate that the deviation of the fluorescence spectra from the spectra in the bulk is less than 1% for crystals with radii smaller than 50 nm but sharply increases to about 10% when the radius increases from about 75 to about 150 nm. When the particle radius changes between 150 and 300 nm, the deviation of the spectra from the bulk case averaged over center location tends to increase slowly from about 10 to about 15%. For a single center, this deviation strongly depends on the location of the center and orientation of its dipole moment. The spectra corresponding to the geometry when the transition dipole is perpendicular to the radial line of the sphere and the emission are collected in the direction perpendicular to the dipole that is least dependent on the size of the crystal and the position of the center. Our results indicate that the information of the exact geometry of the NV-diamond system is critical to understand and control the fluorescence profile, which is of importance to optimize such systems for quantum biosensing applications.

APPENDIX A: THEORETICAL MODEL

In our model, we represent a single NV in a spherical particle with a refractive index of $n_2 = 2.4$ by an electric dipole. The broad NV emission spectrum is represented by emission by 12 point dipoles $\boldsymbol{p} \equiv \boldsymbol{p}_i$ $(i = 0, 1, 2, \ldots, 11)$ corresponding to the NV deexciting via a single photon and multiple phonons as listed in Table I. All electric dipoles are colocated at $\boldsymbol{x}_d$ but each of them oscillates at a specific angular frequency $\omega \equiv \omega_i$ $(i = 0, 1, 2, \ldots, 11)$ as $\exp(-i\omega t)$. The emitted electric and magnetic fields from such a dipole are, respectively,

$$\boldsymbol{E}^d = \frac{1}{4\pi\epsilon_0\epsilon_2} \frac{\exp(ik_2 r_d)}{r_d^3} \left\{ \left(-k_2^2 r_d^2 - 3ik_2 r_d + 3\right) \frac{\boldsymbol{r}_d \cdot \boldsymbol{p}}{r_d^2} \boldsymbol{r}_d \right.$$
$$\left. + \left(k_2^2 r_d^2 + ik_2 r_d - 1\right)\boldsymbol{p} \right\}, \tag{A1a}$$

$$\boldsymbol{H}^d = \frac{\omega k_2}{4\pi} [\boldsymbol{r}_d \times \boldsymbol{p}] \left(\frac{1}{r_d} - \frac{1}{ik_2 r_d^2}\right) \frac{\exp(ik_2 r_d)}{r_d} \tag{A1b}$$

where $\boldsymbol{r}_d = \boldsymbol{x} - \boldsymbol{x}_d$ with $\boldsymbol{x}$ being the field location of interest and $r_d = |\boldsymbol{r}_d|$, k_2 is the wave number, ϵ_0 is the permittivity in vacuum, and $\epsilon_2 = n_2^2$ is the relative permittivity of diamond with $n_2 = 2.4$ the refractive index of diamond.

In a homogeneous medium, the intensity of each wavelength would be proportional to the photon emission probability in the actual spectrum at the same wavelength, which in turn is derived from the emission probabilities. However, the electromagnetic fields transmitted to the surrounding medium (air in this paper) are modified due to the boundary conditions on the surface of the particle and can be obtained by solving Maxwell's equations. In the frequency domain, Maxwell's equations in the internal domain of the nanodiamond and the external domain are

$$\nabla \times \boldsymbol{E}^j = i\omega\mu_0\mu_j \boldsymbol{H}^j, \tag{A2a}$$

$$\nabla \cdot \boldsymbol{E}^j = 0, \tag{A2b}$$

$$\nabla \times \boldsymbol{H}^j = -i\omega\epsilon_0\epsilon_j \boldsymbol{E}^j, \tag{A2c}$$

$$\nabla \cdot \boldsymbol{H}^j = 0 \tag{A2d}$$

where μ_0 is the permeability in vacuum, j refers to the external domain and the nanodiamond domain with $j = 1$ and 2, respectively, and μ_j is the relative permeability of each domain which is set as $\mu_1 = \mu_2 = 1$ in this paper.
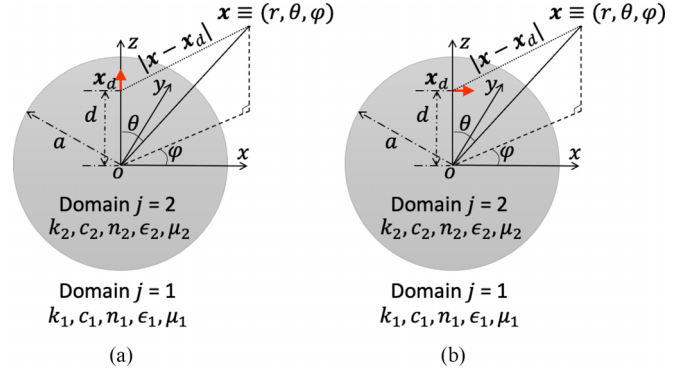

FIG. 9. Sketch of the calculation model for the internal and external electromagnetic fields driven by (a) a vertical or (b) a horizontal electric dipole embedded in a dielectric sphere.

Together with the boundary conditions,

$$\boldsymbol{t}_1 \cdot (\boldsymbol{E}^2 + \boldsymbol{E}^d) = \boldsymbol{t}_1 \cdot \boldsymbol{E}^1, \quad \boldsymbol{t}_2 \cdot (\boldsymbol{E}^2 + \boldsymbol{E}^d) = \boldsymbol{t}_2 \cdot \boldsymbol{E}^1, \tag{A3a}$$

$$\boldsymbol{t}_1 \cdot (\boldsymbol{H}^2 + \boldsymbol{H}^d) = \boldsymbol{t}_1 \cdot \boldsymbol{H}^1, \quad \boldsymbol{t}_2 \cdot (\boldsymbol{H}^2 + \boldsymbol{H}^d) = \boldsymbol{t}_2 \cdot \boldsymbol{H}^1 \tag{A3b}$$

where $\boldsymbol{t}_1$ and $\boldsymbol{t}_2$ are the two independent unit tangential directions on the diamond surface, Maxwell's equations (A2) are solved using the Mie theory, which is detailed in Appendix B.

APPENDIX B: SOLUTION FOR THE ELECTROMAGNETIC FIELDS EMITTED FROM A NV CENTER IN A SPHERICAL DIAMOND PARTICLE

The solution procedure to calculate the electromagnetic fields emitted from a NV center in a spherical diamond particle is given. It is worth noting that to easily and clearly show the calculation procedure and apply the usual setup of a spherical coordinate system, the equivalent electric dipole for the NV center is chosen to locate along the the axis of symmetry (z axis) from which the polar angle is measured in this Appendix. It is straightforward to use the solution given here to get the results presented in the main text via simple coordinate transform and rotation.

To obtain the electromagnetic field radiated from a single NV center in a spherical diamond particle to the external domain, it is convenient to use the spherical coordinate system, (r, θ, φ), the origin of which is at the center of the diamond particle. As shown in Fig. 9, we assign the symmetric axis to be along the z axis which is the polar angle θ measured from. The equivalent electric dipole for the NV center is positioned along the axis of symmetry at $d\boldsymbol{e}_z = d\cos\theta\boldsymbol{e}_r - d\sin\theta\boldsymbol{e}_\theta$. Two situations are considered separately: (i) the vertical dipole when the dipole moment direction is along the symmetric axis (z axis) as $\boldsymbol{p} = p\boldsymbol{e}_z = p\cos\theta\boldsymbol{e}_r - p\sin\theta\boldsymbol{e}_\theta$ as shown in Fig. 9(a) and detailed in Appendix B1 and (ii) the horizontal dipole when the dipole moment direction is perpendicular to the z axis as $\boldsymbol{p} = p\boldsymbol{e}_x = p\sin\theta\cos\varphi\boldsymbol{e}_r + p\cos\theta\cos\varphi\boldsymbol{e}_\theta - p\sin\varphi\boldsymbol{e}_\varphi$ as shown in Fig. 9(b) and detailed in Appendix B2. Here, $\boldsymbol{e}_r$, $\boldsymbol{e}_\theta$, and $\boldsymbol{e}_\varphi$ are the unit vectors along r, θ, and φ directions in the spherical coordinate system, respectively. All the other dipole location and polarization scenarios, such as the cases presented in the main text, can be easily obtained

through coordinate rotation and linear superposition from the above two basic cases.

In the spherical coordinate system, Maxwell's equations in Eq. (A2) are in the form of

$$\frac{1}{r\sin\theta}\left[\frac{\partial}{\partial\theta}\left(E_\varphi^j\sin\theta\right) - \frac{\partial E_\theta^j}{\partial\varphi}\right] = i\omega\mu_0\mu_j H_r^j, \quad \text{(B1a)}$$

$$\frac{1}{r}\left[\frac{1}{\sin\theta}\frac{\partial E_r^j}{\partial\varphi} - \frac{\partial}{\partial r}\left(rE_\varphi^j\right)\right] = i\omega\mu_0\mu_j H_\theta^j, \quad \text{(B1b)}$$

$$\frac{1}{r}\left[\frac{\partial}{\partial r}\left(rE_\theta^j\right) - \frac{\partial E_r^j}{\partial\theta}\right] = i\omega\mu_0\mu_j H_\varphi^j, \quad \text{(B1c)}$$

$$\frac{1}{r\sin\theta}\left[\frac{\partial}{\partial\theta}\left(H_\varphi^j\sin\theta\right) - \frac{\partial H_\theta^j}{\partial\varphi}\right] = -i\omega\epsilon_0\epsilon_j E_r^j, \quad \text{(B2a)}$$

$$\frac{1}{r}\left[\frac{1}{\sin\theta}\frac{\partial H_r^j}{\partial\varphi} - \frac{\partial}{\partial r}\left(rH_\varphi^j\right)\right] = -i\omega\epsilon_0\epsilon_j E_\theta^j, \quad \text{(B2b)}$$

$$\frac{1}{r}\left[\frac{\partial}{\partial r}\left(rH_\theta^j\right) - \frac{\partial H_r^j}{\partial\theta}\right] = -i\omega\epsilon_0\epsilon_j E_\varphi^j. \quad \text{(B2c)}$$

In the above equation, the continuity equations of the electric and magnetic fields are not given as they are satisfied straightforwardly when the Mie solution procedure is used, as demonstrated below.

Before we solve for the reflection and radiation electromagnetic fields in domain 1 and 2, we need to write the fields due to the electric dipole in the spherical coordinate system. From Eq. (A1), we have

$$\boldsymbol{E}^d = \frac{1}{4\pi\epsilon_0\epsilon_2}\frac{\exp(ik_2 r_d)}{r_d^3}\left\{\left(-k_2^2 r_d^2 - 3ik_2 r_d + 3\right)\frac{\boldsymbol{r}_d\cdot\boldsymbol{p}}{r_d^2}\boldsymbol{r}_d\right.$$

$$\left. + \left(k_2^2 r_d^2 + ik_2 r_d - 1\right)\boldsymbol{p}\right\}$$

$$= \frac{1}{4\pi\epsilon_0\epsilon_2}[\boldsymbol{p}\nabla^2 G(\boldsymbol{x},\boldsymbol{x}_d) - (\boldsymbol{p}\cdot\nabla)\nabla G(\boldsymbol{x},\boldsymbol{x}_d)], \quad \text{(B3a)}$$

$$\boldsymbol{H}^d = \frac{\omega k_2}{4\pi}[\boldsymbol{r}_d\times\boldsymbol{p}]\left(\frac{1}{r_d} - \frac{1}{ik_2 r_d^2}\right)\frac{\exp(ik_2 r_d)}{r_d}$$

$$= -\frac{i\omega}{4\pi}[\nabla G(\boldsymbol{x},\boldsymbol{x}_d)\times\boldsymbol{p}] \quad \text{(B3b)}$$

where $G(\boldsymbol{x},\boldsymbol{x}_d)$ is the Green's function for the Helmholtz equation as

$$G(\boldsymbol{x},\boldsymbol{x}_d) = \frac{\exp(ik_2|\boldsymbol{x}-\boldsymbol{x}_d|)}{|\boldsymbol{x}-\boldsymbol{x}_d|}. \quad \text{(B4)}$$

As shown in Fig. 9, $r_d \equiv |\boldsymbol{x}-\boldsymbol{x}_d| = \sqrt{r^2+d^2-2rd\cos\theta}$ based on the cosine theorem. In this case, the free-space Green's function for the Helmholtz equation can be rewritten in terms of (r, d, θ) and asymptotically represented in terms of free spherical multipolar waves, respectively, as

$$G(\boldsymbol{x},\boldsymbol{x}_d) \equiv G(r,\theta;d)$$

$$= \frac{\exp(ik_2\sqrt{r^2+d^2-2rd\cos\theta})}{\sqrt{r^2+d^2-2rd\cos\theta}} \quad \text{(B5)}$$

$$= ik_2\sum_{n=0}^{N}(2n+1)h_n^{(1)}(k_2 r_>)j_n(k_2 r_<)P_n(\cos\theta) \quad \text{(B6)}$$

where $r_> \equiv \max(|\boldsymbol{x}|, d)$, $r_< \equiv \min(|\boldsymbol{x}|, d)$, and $N = k_1 a + 4(k_1 a)^{1/3} + 2$ is the transacted number for the summation [41]. Introducing Eq. (B5) or Eq. (B6) into Eq. (B3) and using the vector calculus formulas in the spherical coordinate system, the fields due to the electric dipole in the spherical coordinate system are obtained.

1. Vertical electric dipole

Let us first solve for the electromagnetic fields as the case illustrated in Fig. 9(a). Introducing Eq. (B5) into Eq. (B3) and using the vector calculus formulas in the spherical coordinate system, the electric and magnetic fields induced by a vertical electric dipole, when $\boldsymbol{p} = p\cos\theta\boldsymbol{e}_r - p\sin\theta\boldsymbol{e}_\theta$, are

$$E_r^d = \frac{1}{4\pi\epsilon_0\epsilon_2}\frac{p}{d}\left\{\frac{\partial^2[r\,G(r,\theta;d)]}{\partial r^2} + k_2^2\,r\,G(r,\theta;d)\right\}, \quad \text{(B7a)}$$

$$E_\theta^d = \frac{1}{4\pi\epsilon_0\epsilon_2}\frac{p}{rd}\frac{\partial^2[r\,G(r,\theta;d)]}{\partial r\partial\theta}, \quad \text{(B7b)}$$

$$E_\varphi^d = 0, \quad \text{(B7c)}$$

$$H_r^d = 0, \quad \text{(B7d)}$$

$$H_\theta^d = 0, \quad \text{(B7e)}$$

$$H_\varphi^d = -\frac{i\omega}{4\pi}\frac{p}{d}\frac{\partial G(r,\theta;d)}{\partial\theta}. \quad \text{(B7f)}$$

Based on the Mie theory [39] by using Debye potentials u and v that satisfy the Helmholtz equation [40,41], we can write the electric and magnetic fields as

$$\boldsymbol{E} = E_0(\boldsymbol{M}_v - i\boldsymbol{N}_u), \quad \text{(B8a)}$$

$$\boldsymbol{H} = E_0\sqrt{\frac{\epsilon_0\epsilon_r}{\mu_0\mu_r}}(-i\boldsymbol{N}_v - \boldsymbol{M}_u) \quad \text{(B8b)}$$

where $E_0 = p/(4\pi\epsilon_0 a^3)$,

$$\boldsymbol{M}_u = \nabla\times(\boldsymbol{r}u), \quad \boldsymbol{M}_v = \nabla\times(\boldsymbol{r}v),$$

$$\nabla\times\boldsymbol{M}_u = \omega(\epsilon_0\epsilon_r\mu_0\mu_r)^{\frac{1}{2}}\boldsymbol{N}_u,$$

$$\nabla\times\boldsymbol{M}_v = \omega(\epsilon_0\epsilon_r\mu_0\mu_r)^{\frac{1}{2}}\boldsymbol{N}_v,$$

$$\nabla\times\boldsymbol{N}_u = \omega(\epsilon_0\epsilon_r\mu_0\mu_r)^{\frac{1}{2}}\boldsymbol{M}_u,$$

$$\nabla\times\boldsymbol{N}_v = \omega(\epsilon_0\epsilon_r\mu_0\mu_r)^{\frac{1}{2}}\boldsymbol{M}_v,$$

$$\nabla\times\boldsymbol{E} = i\omega\mu_0\mu_r\boldsymbol{H}, \quad \nabla\times\boldsymbol{H} = -i\omega\epsilon_0\epsilon_r\boldsymbol{E}. \quad \text{(B9)}$$

The full components of $\boldsymbol{M}_u$ and $\boldsymbol{N}_u$ are, respectively,

$$M_{u_r} = 0, \quad M_{u_\theta} = \frac{1}{r\sin\theta}\frac{\partial(ru)}{\partial\varphi}, \quad M_{u_\varphi} = -\frac{1}{r}\frac{\partial(ru)}{\partial\theta},$$
$$\text{(B10a)}$$

$$N_{u_r} = \frac{1}{k}\frac{\partial^2(ru)}{\partial r^2} + kru, \quad N_{u_\theta} = \frac{1}{kr}\frac{\partial^2(ru)}{\partial r\partial\theta},$$

$$N_{u_\varphi} = \frac{1}{kr\sin\theta}\frac{\partial^2(ru)}{\partial r\partial\varphi}. \quad \text{(B10b)}$$

The above formulations can also be used to get the components of $\boldsymbol{M}_v$ and $\boldsymbol{N}_v$ when potential u is replaced by potential v.

As Debye potentials u and v satisfy the Helmholtz equation, let us consider a scalar wave equation for function ϕ with

wave number k:

$$\nabla^2 \phi + k^2 \phi = 0 \tag{B11}$$

where ϕ represents either potential u or v. Equation (B11) is variable separable in the spherical coordinate system, and its elementary solutions are

$$\phi_{(l,n)} = \sum_{n=0}^{\infty} \sum_{l=-n}^{l=n} C_{l,n} \cos(l\varphi) P_n^l(\cos\theta) z_n(kr), \tag{B12a}$$

$$\phi_{(l,n)} = \sum_{n=0}^{\infty} \sum_{l=-n}^{l=n} D_{l,n} \sin(l\varphi) P_n^l(\cos\theta) z_n(kr) \tag{B12b}$$

where l and n are integers ($n \geqslant l \geqslant 0$), $P_n^l(\cos\theta)$ is an associated Legendre polynomial, and $z_n(kr)$ is the spherical Bessel function of any kind. The following rules are applied to determine the choice of function $z_n(kr)$. In the bounded domain with origin within it, $j_n(kr)$, the spherical Bessel function of the first kind is used as $j_n(kr)$ is finite at the origin. In the bounded domain excluding origin, both $j_n(kr)$ and $y_n(kr)$, the spherical Bessel functions of the first and second kinds, are needed. In the unbounded external domain, for the scattered or radiation field, $h_n^{(1)} = j_n(kr) + iy_n(kr)$ is used as $ikh_n^{(1)} \sim i^n \exp(ikr)/r$.

It is worth noting that the two Debye potentials, u and v, correspond to $\cos(l\varphi)$ and $\sin(l\varphi)$ formulations in Eq. (B12), respectively. Nevertheless, according to Eq. (B7), the fields driven by a vertical electric dipole in a sphere do not depend on φ. As such, only terms with $l = 0$ in Eq. (B12) are needed, which means only one potential is needed for each domain. Let us use potential u:

$$u_{(0,n)}^1 = \sum_{n=0}^{N} C_{(0,n)}^1 P_n(\cos\theta) h_n^{(1)}(k_1 r), \tag{B13a}$$

$$u_{(0,n)}^2 = \sum_{n=0}^{N} C_{(0,n)}^2 P_n(\cos\theta) j_n(k_2 r) \tag{B13b}$$

for the external and internal domain, respectively, where the $C_{(0,n)}^1$ and $C_{(0,n)}^2$ are determined by the boundary conditions. Introducing Eq. (B13) into Eq. (B8) and using Eq. (B10), we obtain

$$E_r^1 = E_0 \sum_{n=0}^{N} C_{(0,n)}^1 (-i) \frac{n(n+1)}{k_1 r} h_n^{(1)}(k_1 r) P_n(\cos\theta), \tag{B14a}$$

$$E_\theta^1 = E_0 \sum_{n=0}^{N} C_{(0,n)}^1 (-i) \frac{1}{k_1 r} \big[(n+1) h_n^{(1)}(k_1 r) - k_1 r h_{n+1}^{(1)}(k_1 r) \big] P_n^1(\cos\theta), \tag{B14b}$$

$$H_\varphi^1 = \frac{E_0}{\omega\mu_0} \sum_{n=0}^{N} C_{(0,n)}^1 \frac{k_1}{\mu_1} h_n^{(1)}(k_1 r) P_n^1(\cos\theta), \tag{B14c}$$

and $E_\varphi^1 = H_r^1 = H_\theta^1 = 0$. Also,

$$E_r^2 = E_0 \sum_{n=0}^{N} C_{(0,n)}^2 (-i) \frac{n(n+1)}{k_2 r} j_n(k_2 r) P_n(\cos\theta), \tag{B15a}$$

$$E_\theta^2 = E_0 \sum_{n=0}^{N} C_{(0,n)}^2 (-i) \frac{1}{k_2 r} \big[(n+1) j_n(k_2 r) - k_2 r j_{n+1}(k_2 r) \big] P_n^1(\cos\theta), \tag{B15b}$$

$$H_\varphi^2 = \frac{E_0}{\omega\mu_0} \sum_{n=0}^{N} C_{(0,n)}^2 \frac{k_2}{\mu_2} j_n(k_2 r) P_n^1(\cos\theta), \tag{B15c}$$

and $E_\varphi^2 = H_r^2 = H_\theta^2 = 0$.

To get $C_{(0,n)}^1$ and $C_{(0,n)}^2$, the boundary conditions across the sphere surface

$$E_\theta^1 = E_\theta^2 + E_\theta^d \quad \text{when } r = a, \tag{B16a}$$

$$H_\varphi^1 = H_\varphi^2 + H_\varphi^d \quad \text{when } r = a \tag{B16b}$$

are used. Introducing Eq. (B6) into Eq. (B7) and setting $r = a$, we have

$$E_\theta^d \Big|_{r=a} = \frac{1}{4\pi\epsilon_0\epsilon_2} \frac{p}{ad} ik_2 \sum_{n=0}^{N} (2n+1) j_n(k_2 d) P_n^1(\cos\theta) \\ \times \frac{d\big[r h_n^{(1)}(k_2 r) \big]}{dr} \Big|_{r=a}, \tag{B17a}$$

$$H_\varphi^d \Big|_{r=a} = -\frac{i\omega}{4\pi} \frac{p}{d} ik_2 \sum_{n=0}^{N} (2n+1) h_n^{(1)}(k_2 a) j_n(k_2 d) \\ \times P_n^1(\cos\theta). \tag{B17b}$$

Letting $r = a$ in Eqs. (B14) and (B15), and introducing the results and Eq. (B17) into Eq. (B16), we obtain a 2×2 linear system to solve for the unknown coefficients $C_{(0,n)}^1$ and $C_{(0,n)}^2$ which can be then introduced into Eqs. (B14) and (B15) to calculate the fields inside, outside the sphere and on the sphere surface.

2. Horizontal electric dipole

Let us turn to solve for the electromagnetic fields as the case illustrated in Fig. 9(b). Introducing Eq. (B5) into Eq. (B3) and using the vector calculus formulas in the spherical coordinate system, the radial components of the electric and magnetic fields induced by a horizontal electric dipole when $\boldsymbol{p} = p\sin\theta\cos\varphi \boldsymbol{e}_r + p\cos\theta\cos\varphi \boldsymbol{e}_\theta - p\sin\varphi \boldsymbol{e}_\varphi$ are

$$E_r^d = -\frac{1}{4\pi\epsilon_0\epsilon_2} \frac{p}{r} \frac{\partial}{\partial\theta} \left\{ \frac{\partial[G(r,\theta;d)]}{\partial d} + \frac{1}{d} G(r,\theta;d) \right\} \\ \times \cos\varphi, \tag{B18a}$$

$$H_r^d = \frac{i\omega}{4\pi} \frac{p}{r} \frac{\partial G(r,\theta;d)}{\partial\theta} \sin\varphi. \tag{B18b}$$

Following the same solution procedure shown in the previous section and considering that the electromagnetic fields given in Eq. (B18) are functions of $\sin\varphi$ and $\cos(\varphi)$, only the terms when $l = 1$ from the elementary solutions in Eq. (B12) are needed for the Debye potentials. As such, the following Debye potentials

$$u_{(1,n)}^1 = \cos\varphi \sum_{n=1}^{N} C_{(1,n)}^1 h_n^{(1)}(k_1 r) P_n^1(\cos\theta), \quad \text{(B19a)}$$

$$v_{(1,n)}^1 = -\sin\varphi \sum_{n=1}^{N} D_{(1,n)}^1 h_n^{(1)}(k_1 r) P_n^1(\cos\theta), \quad \text{(B19b)}$$

$$u_{(1,n)}^2 = \cos\varphi \sum_{n=1}^{N} C_{(1,n)}^2 j_n(k_1 r) P_n^1(\cos\theta), \quad \text{(B19c)}$$

$$v_{(1,n)}^2 = -\sin\varphi \sum_{n=1}^{N} D_{(1,n)}^2 j_n(k_1 r) P_n^1(\cos\theta) \quad \text{(B19d)}$$

for the external (with superscript 1) and internal domain (with superscript 2), respectively, are used where $C_{(1,n)}^1$, $D_{(1,n)}^1$, $C_{(1,n)}^2$, and $D_{(1,n)}^2$ are unknowns to be determined via boundary conditions.

Introducing Eq. (B19) into Eq. (B8) and using Eq. (B10), we obtain

$$E_r^1 = E_0 \cos\varphi \sum_{n=1}^{N} C_{(1,n)}^1 (-i) \frac{n(n+1)}{k_1 r} h_n^{(1)}(k_1 r) P_n^1(\cos\theta), \quad \text{(B20a)}$$

$$E_\theta^1 = E_0 \cos\varphi \sum_{n=1}^{N} C_{(1,n)}^1 (-i) \frac{1}{k_1 r} \left[(n+1)h_n^{(1)}(k_1 r) - k_1 r h_{n+1}^{(1)}(k_1 r)\right] \frac{dP_n^1(\cos\theta)}{d\theta}$$

$$+ E_0 \cos\varphi \sum_{n=1}^{N} D_{(1,n)}^1 (-1) h_n^{(1)}(k_1 r) \frac{P_n^1(\cos\theta)}{\sin\theta}, \quad \text{(B20b)}$$

$$E_\varphi^1 = E_0 \sin\varphi \sum_{n=1}^{N} C_{(1,n)}^1 (i) \frac{1}{k_1 r} \left[(n+1)h_n^{(1)}(k_1 r) - k_1 r h_{n+1}^{(1)}(k_1 r)\right] \frac{P_n^1(\cos\theta)}{\sin\theta}$$

$$+ E_0 \sin\varphi \sum_{n=1}^{N} D_{(1,n)}^1 h_n^{(1)}(k_1 r) \frac{dP_n^1(\cos\theta)}{d\theta}, \quad \text{(B20c)}$$

$$H_r^1 = \frac{E_0}{\omega\mu_0} \sin\varphi \sum_{n=1}^{N} D_{(1,n)}^1 (i) \frac{k_1}{\mu_1} \frac{n(n+1)}{k_1 r} h_n^{(1)}(k_1 r) P_n^1(\cos\theta), \quad \text{(B21a)}$$

$$H_\theta^1 = \frac{E_0}{\omega\mu_0} \sin\varphi \sum_{n=1}^{N} C_{(1,n)}^1 \frac{k_1}{\mu_1} h_n^{(1)}(k_1 r) \frac{P_n^1(\cos\theta)}{\sin\theta}$$

$$+ \frac{E_0}{\omega\mu_0} \sin\varphi \sum_{n=1}^{N} D_{(1,n)}^1 (i) \frac{k_1}{\mu_1} \frac{1}{k_1 r} \left[(n+1)h_n^{(1)}(k_1 r) - k_1 r h_{n+1}^{(1)}(k_1 r)\right] \frac{dP_n^1(\cos\theta)}{d\theta}, \quad \text{(B21b)}$$

$$H_\varphi^1 = \frac{E_0}{\omega\mu_0} \cos\varphi \sum_{n=1}^{N} C_{(1,n)}^1 \frac{k_1}{\mu_1} h_n^{(1)}(k_1 r) \frac{dP_n^1(\cos\theta)}{d\theta}$$

$$+ \frac{E_0}{\omega\mu_0} \cos\varphi \sum_{n=1}^{N} D_{(1,n)}^1 (i) \frac{k_1}{\mu_1} \frac{1}{k_1 r} \left[(n+1)h_n^{(1)}(k_1 r) - k_1 r h_{n+1}^{(1)}(k_1 r)\right] \frac{P_n^1(\cos\theta)}{\sin\theta}. \quad \text{(B21c)}$$

Also

$$E_r^2 = E_0 \cos\varphi \sum_{n=1}^{N} C_{(1,n)}^2 (-i) \frac{n(n+1)}{k_2 r} j_n(k_2 r) P_n^1(\cos\theta), \quad \text{(B22a)}$$

$$E_\theta^2 = E_0 \cos\varphi \sum_{n=1}^{N} C_{(1,n)}^2 (-i) \frac{1}{k_2 r} [(n+1)j_n(k_2 r) - k_2 r j_{n+1}(k_2 r)] \frac{dP_n^1(\cos\theta)}{d\theta}$$

$$+ E_0 \cos\varphi \sum_{n=1}^{N} D_{(1,n)}^2 (-1) j_n(k_2 r) \frac{P_n^1(\cos\theta)}{\sin\theta}, \quad \text{(B22b)}$$

$$E_\varphi^2 = E_0 \sin\varphi \sum_{n=1}^{N} C_{(1,n)}^2 (i) \frac{1}{k_2 r} [(n+1)j_n(k_2 r) - k_2 r j_{n+1}(k_2 r)] \frac{P_n^1(\cos\theta)}{\sin\theta} + E_0 \sin\varphi \sum_{n=1}^{N} D_{(1,n)}^2 j_n(k_2 r) \frac{dP_n^1(\cos\theta)}{d\theta}, \quad \text{(B22c)}$$

$$H_r^1 = \frac{E_0}{\omega\mu_0}\sin\varphi \sum_{n=1}^{N} D_{(1,n)}^2(i)\frac{k_2}{\mu_2}\frac{n(n+1)}{k_2 r}j_n(k_2 r)P_n^1(\cos\theta),$$ (B23a)

$$H_\theta^1 = \frac{E_0}{\omega\mu_0}\sin\varphi \sum_{n=1}^{N} C_{(1,n)}^2\frac{k_2}{\mu_2}j_n(k_2 r)\frac{P_n^1(\cos\theta)}{\sin\theta}$$

$$+ \frac{E_0}{\omega\mu_0}\sin\varphi \sum_{n=1}^{N} D_{(1,n)}^2(i)\frac{k_2}{\mu_2}\frac{1}{k_2 r}[(n+1)j_n(k_2 r) - k_2 r j_{n+1}(k_2 r)]\frac{dP_n^1(\cos\theta)}{d\theta},$$ (B23b)

$$H_\varphi^1 = \frac{E_0}{\omega\mu_0}\cos\varphi \sum_{n=1}^{N} C_{(1,n)}^2\frac{k_2}{\mu_2}j_n(k_2 r)\frac{dP_n^1(\cos\theta)}{d\theta}$$

$$+ \frac{E_0}{\omega\mu_0}\cos\varphi \sum_{n=1}^{N} D_{(1,n)}^2(i)\frac{k_2}{\mu_2}\frac{1}{k_2 r}[(n+1)j_n(k_2 r) - k_2 r j_{n+1}(k_2 r)]\frac{P_n^1(\cos\theta)}{\sin\theta}.$$ (B23c)

Once the coefficients $C_{(1,n)}^1$, $D_{(1,n)}^1$, $C_{(1,n)}^2$, and $D_{(1,n)}^2$ are found, the electromagnetic fields in both domains are determined. To get those coefficients, the boundary conditions for the tangential components of the electric and magnetic fields due to the electric dipole on the sphere surface when $r = a$ are needed, which can be found by using Maxwell's equations and the radial components in Eq. (B18) [42]. Introducing Eq. (B1b) in Eq. (B2c), for the sphere domain, we get

$$\frac{\partial^2}{\partial r^2}(rE_\varphi^d) + k_2^2(rE_\varphi^d) = \frac{1}{\sin\theta}\frac{\partial}{\partial r}\left(\frac{\partial E_r^d}{\partial\varphi}\right) - i\omega\mu_0\mu_2\frac{\partial H_r^d}{\partial\theta}.$$ (B24)

The right-hand side of Eq. (B24) can be obtained by using the results from introducing Eq. (B6) into Eq. (B18):

$$\frac{1}{\sin\theta}\frac{\partial}{\partial r}\left(\frac{\partial E_r^d}{\partial\varphi}\right)$$

$$= \frac{p\sin\varphi}{4\pi\epsilon_0\epsilon_2}\frac{ik_2}{d}\sum_{n=1}^{N}(2n+1)\frac{d}{dr}\left[\frac{h_n^{(1)}(k_2 r)}{r}\right]$$

$$\times [(n+1)j_n(k_2 d) - k_2 d\, j_{n+1}(k_2 d)]\frac{P_n^1(\cos\theta)}{\sin\theta},$$ (B25)

and

$$-i\omega\mu_0\mu_2\frac{\partial H_r^d}{\partial\theta} = \frac{ipk_2^3\sin\varphi}{4\pi\epsilon_0\epsilon_2}\sum_{n=1}^{N}(2n+1)\frac{h_n^{(1)}(k_2 r)}{r}j_n(k_2 d)$$

$$\times \frac{dP_n^1(\cos\theta)}{d\theta},$$ (B26)

in which the situation for the fields on the sphere surface when $r \to a > d$ is implied. When comparing the left-hand side of Eq. (B24) and Eqs. (B25) and (B26), we notice that we can get the tangential component, E_φ^d, by solving the following two ordinary differential equations:

$$\frac{d^2 g_1(r)}{\partial r^2} + k_2^2 g_1(r) = \frac{d}{dr}\left[\frac{h_n^{(1)}(k_2 r)}{r}\right],$$ (B27)

$$\frac{d^2 g_2(r)}{\partial r^2} + k_2^2 g_2(r) = \frac{h_n^{(1)}(k_2 r)}{r}.$$ (B28)

The solutions to the above two equations are, respectively,

$$g_1(r) = \frac{1}{n(n+1)}\frac{d}{dr}\left[rh_n^{(1)}(k_2 r)\right]$$

$$= \frac{1}{n(n+1)}\left[(n+1)h_n^{(1)}(k_2 r) - k_2 r\, h_{n+1}^{(1)}(k_2 r)\right],$$ (B29)

$$g_2(r) = \frac{1}{n(n+1)}rh_n^{(1)}(k_2 r).$$ (B30)

As such,

$$E_\varphi^d = \frac{p\sin\varphi}{4\pi\epsilon_0\epsilon_2}\frac{ik_2}{rd}\sum_{n=1}^{N}\frac{2n+1}{n(n+1)}\frac{d}{dr}[rh_n^{(1)}(k_2 r)]$$

$$\times [(n+1)j_n(k_2 d) - k_2 d\, j_{n+1}(k_2 d)]\frac{P_n^1(\cos\theta)}{\sin\theta}$$

$$+ \frac{p\sin\varphi}{4\pi\epsilon_0\epsilon_2}ik_2^3\sum_{n=1}^{N}\frac{2n+1}{n(n+1)}h_n^{(1)}(k_2 r)j_n(k_2 d)\frac{dP_n^1(\cos\theta)}{d\theta}.$$ (B31)

Introducing Eq. (B6) into Eq. (B18) and substituting that result and Eq. (B31) into Eq. (B1b), we have

$$H_\theta^d = \frac{1}{i\omega\mu_0\mu_2}\left[\frac{1}{r\sin\theta}\frac{\partial E_r^d}{\partial\varphi} - \frac{1}{r}\frac{\partial(rE_\varphi^d)}{\partial r}\right]$$

$$= \frac{p\omega\sin\varphi}{4\pi}\frac{1}{rd}\sum_{n=1}^{N}\frac{2n+1}{n(n+1)}k_2 rh_n^{(1)}(k_2 r)$$

$$\times [(n+1)j_n(k_2 d) - k_2 d\, j_{n+1}(k_2 d)]\frac{P_n^1(\cos\theta)}{\sin\theta}$$

$$- \frac{p\omega\sin\varphi}{4\pi}\frac{k_2}{r}\sum_{n=1}^{N}\frac{2n+1}{n(n+1)}\frac{d}{dr}[rh_n^{(1)}(k_2 r)]$$

$$\times j_n(k_2 d)\frac{dP_n^1(\cos\theta)}{d\theta}.$$ (B32)

As the tangential components of the electric and magnetic fields are continuous across the sphere surface, we have

$$E_\varphi^1 = E_\varphi^2 + E_\varphi^d \quad \text{when } r = a, \tag{B33a}$$

$$H_\theta^1 = H_\theta^2 + H_\theta^d \quad \text{when } r = a. \tag{B33b}$$

Comparing the expressions in Eqs. (B20c), (B21b), (B22c), and (B23b) and those in Eqs. (B31) and (B32), we obtain a 4×4 linear system to solve for the unknown coefficients $C_{(1,n)}^1$, $D_{(1,n)}^1$, $C_{(1,n)}^2$, and $D_{(1,n)}^2$ that can be introduced back into Eqs. (B20) and (B23) to calculate the fields inside the sphere, outside the sphere, and on the sphere surface.

In Fig. 10, we showed the electromagnetic fields obtained by the asymptotic approximations detailed in Appendix B, and compared them with the results gotten by the in-house built field only surface integral method [43,49–53]. Good agreement has been found between the results obtained by the different methods mentioned above.
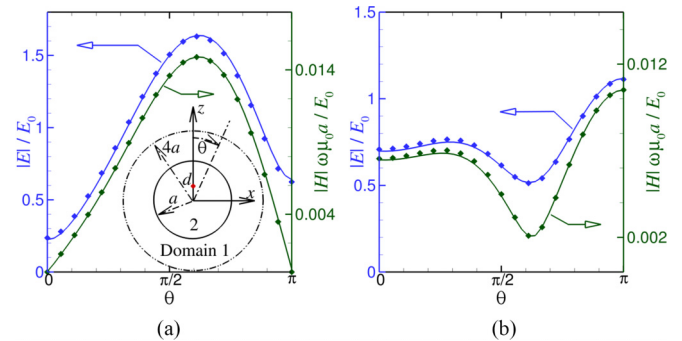

FIG. 10. Good agreement has been found for the electromagnetic fields between the results obtained by the asymptotic approximations shown in Appendix B (solid lines), by the in-house built field only surface integral method [43] (symbols) when $a = 200$ nm, $d = 50$ nm, $n_1 = 1$, $n_2 = 2.4$, $E_0 = p/(4\pi\epsilon_0 a^3)$, and $\lambda = 708$ nm: (a) a vertical electric dipole and (b) a horizontal electric dipole. The curves plotted are the magnitudes of the electromagnetic fields along the circle concentric with the spherical particle with radius as $4a$ on the xz plane [as shown in the inset of Fig. 10(a)].

[1] A. N. Schechter, Hemoglobin research and the origins of molecular medicine, Blood **112**, 3927 (2008).

[2] L. P. McGuinness, Y. Yan, A. Stacey, D. A. Simpson, L. T. Hall, D. Maclaurin, S. Prawer, P. Mulvaney, J. Wrachtrup, F. Caruso, R. E. Scholten, and L. C. L. Hollenberg, Quantum measurement and orientation tracking of fluorescent nanodiamonds inside living cells, Nat. Nanotechnol. **6**, 358 (2011).

[3] C. Thomas and A. B. Lumb, Physiology of haemoglobin, Continuing Education in Anaesthesia Critical Care and Pain **12**, 251 (2012).

[4] Y. Wang, M. Jin, G. Chen, X. Cui, Y. Zhang, M. Li, Y. Liao, X. Zhang, G. Qin, F. Yan, A. A. El-Aty, and J. Wang, Bio-barcode detection technology and its research applications: A review, J. Adv. Res. **20**, 23 (2019).

[5] Y. Wu, F. Jelezko, M. B. Plenio, and T. Weil, Diamond quantum devices in biology, Angew. Chem., Int. Ed. **55**, 6586 (2016).

[6] V. E. Tarasov, Quantum nanotechnology, Int. J. Nanosci. **08**, 337 (2009).

[7] A. Laucht, F. Hohls, N. Ubbelohde, M. F. Gonzalez-Zalba, D. J. Reilly, S. Stobbe, T. Schröder, P. Scarlino, J. V. Koski, A. Dzurak, C.-H. Yang, J. Yoneda, F. Kuemmeth, H. Bluhm, J. Pla, C. Hill, J. Salfi, A. Oiwa, J. T. Muhonen, E. Verhagen, M. D. LaHaye, H. H. Kim, A. W. Tsen, D. Culcer, A. Geresdi, J. A. Mol, V. Mohan, P. K. Jain, and J. Baugh, Roadmap on quantum nanotechnologies, Nanotechnology **32**, 162003 (2021).

[8] A. J. Heinrich, W. D. Oliver, L. M. K. Vandersypen, A. Ardavan, R. Sessoli, D. Loss, A. B. Jayich, J. Fernandez-Rossier, A. Laucht, and A. Morello, Quantum-coherent nanoscience, Nat. Nanotechnol. **16**, 1318 (2021).

[9] M. L. Cohen, Essay: Fifty Years of Condensed Matter Physics, Phys. Rev. Lett. **101**, 250001 (2008).

[10] Z. Ou, A. Kim, W. Huang, P. V. Braun, X. Li, and Q. Chen, Reconfigurable nanoscale soft materials, Curr. Opin. Solid State Mater. Sci. **23**, 41 (2019).

[11] A. Bachtold, J. Moser, and M. I. Dykman, Mesoscopic physics of nanomechanical systems, Rev. Mod. Phys. **94**, 045005 (2022).

[12] R. Schirhagl, K. Chang, M. Loretz, and C. L. Degen, Nitrogen-vacancy centers in diamond: Nanoscale sensors for physics and biology, Annu. Rev. Phys. Chem. **65**, 83 (2014).

[13] M. H. Alkahtani, F. Alghannam, L. Jiang, A. Almethen, A. A. Rampersaud, R. Brick, C. L. Gomes, M. O. Scully, and P. R. Hemmer, Fluorescent nanodiamonds: Past, present, and future, Nanophotonics **7**, 1423 (2018).

[14] M. Radtke, E. Bernardi, A. Slablab, R. Nelz, and E. Neu, Nanoscale sensing based on nitrogen vacancy centers in single crystal diamond and nanodiamonds: Achievements and challenges, Nano Futures **3**, 042004 (2019).

[15] I. Aharonovich, A. D. Greentree, and S. Prawer, Diamond photonics, Nat. Photonics **5**, 397 (2011).

[16] Y. Zhu, J. Li, W. Li, Y. Zhang, X. Yang, N. Chen, Y. Sun, Y. Zhao, C. Fan, and Q. Huang, The biocompatibility of nanodiamonds and their application in drug delivery systems, Theranostics **2**, 302 (2012).

[17] V. Vaijayanthimala, P.-Y. Cheng, S.-H. Yeh, K.-K. Liu, C.-H. Hsiao, J.-I. Chao, and H.-C. Chang, The long-term stability and biocompatibility of fluorescent nanodiamond as an in vivo contrast agent, Biomaterials **33**, 7794 (2012).

[18] H.-S. Jung, K.-J. Cho, S.-J. Ryu, Y. Takagi, P. A. Roche, and K. C. Neuman, Biocompatible fluorescent nanodiamonds as multifunctional optical probes for latent fingerprint detection, ACS Applied Materials and Interfaces **12**, 6641 (2020).

[19] J. R. Maze, P. L. Stanwix, J. S. Hodges, S. Hong, J. M. Taylor, P. Cappellaro, L. Jiang, M. V. G. Dutt, E. Togan, A. S. Zibrov, A. Yacoby, R. L. Walsworth, and M. D. Lukin, Nanoscale magnetic sensing with an individual electronic spin in diamond, Nature (London) **455**, 644 (2008).

[20] D. Bai, M. H. Huynh, D. A. Simpson, P. Reineck, S. A. Vahid, A. D. Greentree, S. Foster, H. Ebendorff-Heidepriem, and B. C. Gibson, Fluorescent diamond microparticle doped glass fiber for magnetic field sensing, APL Mater. **8**, 081102 (2020).

[21] F. Dolde, H. Fedder, M. W. Doherty, T. Nöbauer, F. Rempp, G. Balasubramanian, T. Wolf, F. Reinhard, L. C. L. Hollenberg,

F. Jelezko, and J. Wrachtrup, Electric-field sensing using single diamond spins, Nat. Phys. **7**, 459 (2011).

[22] J.-P. Tetienne, N. Dontschuk, D. A. Broadway, A. Stacey, D. A. Simpson, and L. C. L. Hollenberg, Quantum imaging of current flow in graphene, Sci. Adv. **3**, e1602429 (2017).

[23] G. Kucsko, P. C. Maurer, N. Y. Yao, M. Kubo, H. J. Noh, P. K. Lo, H. Park, and M. D. Lukin, Nanometre-scale thermometry in a living cell, Nature (London) **500**, 54 (2013).

[24] A. Khalid, D. Bai, A. N. Abraham, A. Jadhav, D. Linklater, A. Matusica, D. Nguyen, B. J. Murdoch, N. Zakhartchouk, C. Dekiwadia, P. Reineck, D. Simpson, A. K. Vidanapathirana, S. Houshyar, C. A. Bursill, E. P. Ivanova, and B. C. Gibson, Electrospun nanodiamond–silk fibroin membranes: A multifunctional platform for biosensing and wound-healing applications, ACS Applied Materials and Interfaces **12**, 48408 (2020).

[25] M. W. Doherty, V. V. Struzhkin, D. A. Simpson, L. P. McGuinness, Y. Meng, A. Stacey, T. J. Karle, R. J. Hemley, N. B. Manson, L. C. Hollenberg, and S. Prawer, Electronic Properties and Metrology Applications of the Diamond NV-Center Under Pressure, Phys. Rev. Lett. **112**, 047601 (2014).

[26] T. Plakhotnik, M. W. Doherty, J. H. Cole, R. Chapman, and N. B. Manson, All-optical thermometry and thermal properties of the optically detected spin resonances of the NV–center in nanodiamond, Nano Lett. **14**, 4989 (2014).

[27] A. H. Heffernan, A. D. Greentree, and B. C. Gibson, Nanodiamond arrays on glass for quantification and fluorescence characterisation, Sci. Rep. **7**, 9252 (2017).

[28] M. Capelli, A. Heffernan, T. Ohshima, H. Abe, J. Jeske, A. Hope, A. Greentree, P. Reineck, and B. Gibson, Increased nitrogen-vacancy centre creation yield in diamond through electron beam irradiation at high temperature, Carbon **143**, 714 (2019).

[29] E. R. Wilson, L. M. Parker, A. Orth, N. Nunn, M. Torelli, O. Shenderova, B. C. Gibson, and P. Reineck, The effect of particle size on nanodiamond fluorescence and colloidal properties in biological media, Nanotechnology **30**, 385704 (2019).

[30] M. Capelli, L. Lindner, T. Luo, J. Jeske, H. Abe, S. Onoda, T. Ohshima, B. Johnson, D. A. Simpson, A. Stacey, P. Reineck, B. C. Gibson, and A. D. Greentree, Proximal nitrogen reduces the fluorescence quantum yield of nitrogen-vacancy centres in diamond, New J. Phys. **24**, 033053 (2022).

[31] A. S. Zalogina, R. S. Savelev, E. V. Ushakova, G. P. Zograf, F. E. Komissarenko, V. A. Milichko, S. V. Makarov, D. A. Zuev, and I. V. Shadrivov, Purcell effect in active diamond nanoantennas, Nanoscale **10**, 8721 (2018).

[32] H.-Q. Zhao, M. Fujiwara, and S. Takeuchi, Suppression of fluorescence phonon sideband from nitrogen vacancy centers in diamond nanocrystals by substrate effect, Opt. Express **20**, 15628 (2012).

[33] S. Yanagimoto, N. Yamamoto, T. Sannomiya, and K. Akiba, Purcell effect of nitrogen-vacancy centers in nanodiamond coupled to propagating and localized surface plasmons revealed by photon-correlation cathodoluminescence, Phys. Rev. B **103**, 205418 (2021).

[34] J. Riedrich-Möller, S. Pezzagna, J. Meijer, C. Pauly, F. Mücklich, M. Markham, A. M. Edmonds, and C. Becher, Nanoimplantation and purcell enhancement of single nitrogen-vacancy centers in photonic crystal cavities in diamond, Appl. Phys. Lett. **106**, 221103 (2015).

[35] H. Kaupp, T. Hümmer, M. Mader, B. Schlederer, J. Benedikter, P. Haeusser, H.-C. Chang, H. Fedder, T. W. Hänsch, and D. Hunger, Purcell-Enhanced Single-Photon Emission from Nitrogen-Vacancy Centers Coupled to a Tunable Microcavity, Phys. Rev. Applied **6**, 054010 (2016).

[36] G. Alagappan, L. A. Krivitsky, and C. E. Png, Diamond in a nanopocket: A new route to a strong Purcell effect, ACS Omega **3**, 4733 (2018).

[37] G. Davies and M. F. Hamer, Optical studies of the 1.945eV vibronic band in diamond, Proc. R. Soc. Lond. A. **348**, 285 (1976).

[38] C.-H. Su, A. D. Greentree, and L. C. L. Hollenberg, Towards a picosecond transform-limited nitrogen-vacancy based single photon source, Opt. Express **16**, 6240 (2008).

[39] G. Mie, Beiträge zur optik trüber medien, speziell kolloidaler metallösungen, Ann. Phys. (Leipzig) **330**, 377 (1908).

[40] H. C. van de Hulst, *Light Scattering by Small Particles* (Wiley, New York, 1957).

[41] C. F. Bohren and D. R. Huffman, *Absorption and Scattering of Light by Small Particles* (Wiley, New York, 1998).

[42] D. Margetis, Radiation of horizontal electric dipole on large dielectric sphere, J. Math. Phys. **43**, 3162 (2002).

[43] Q. Sun and E. Klaseboer, A non-singular, field-only surface integral method for interactions between electric and magnetic dipoles and nano-structures, Ann. Phys. (NY) **534**, 2100397 (2022).

[44] F. A. Inam, M. D. W. Grogan, M. Rollings, T. Gaebel, J. M. Say, C. Bradac, T. A. Birks, W. J. Wadsworth, S. Castelletto, J. R. Rabeau, and M. J. Steel, Emission and nonradiative decay of nanodiamond NV centers in a low refractive index environment, ACS Nano **7**, 3833 (2013).

[45] See Supplemental Material at http://link.aps.org/supplemental/10.1103/PhysRevA.107.013720 for overall and normalized photon counts.

[46] T. Plakhotnik and H. Aman, NV-centers in nanodiamonds: How good they are, Diam. Relat. Mater. **82**, 87 (2018).

[47] M. Almokhtar, M. Fujiwara, H. Takashima, and S. Takeuchi, Numerical simulations of nanodiamond nitrogen-vacancy centers coupled with tapered optical fibers as hybrid quantum nanophotonic devices, Opt. Express **22**, 20045 (2014).

[48] M. W. Doherty, N. B. Manson, P. Delaney, F. Jelezko, J. Wrachtrup, and L. C. Hollenberg, The nitrogen-vacancy colour centre in diamond, Phys. Rep. **528**, 1 (2013).

[49] E. Klaseboer, Q. Sun, and D. Y. C. Chan, Nonsingular field-only surface integral equations for electromagnetic scattering, IEEE Trans. Antennas Propagat. **65**, 972 (2017).

[50] Q. Sun, E. Klaseboer, and D. Y. C. Chan, Robust multiscale field-only formulation of electromagnetic scattering, Phys. Rev. B **95**, 045137 (2017).

[51] Q. Sun, E. Klaseboer, A. J. Yuffa, and D. Y. C. Chan, Field-only surface integral equations: Scattering from a perfect electric conductor, J. Opt. Soc. Am. A **37**, 276 (2020).

[52] Q. Sun, E. Klaseboer, A. J. Yuffa, and D. Y. C. Chan, Field-only surface integral equations: Scattering from a dielectric body, J. Opt. Soc. Am. A **37**, 284 (2020).

[53] E. Klaseboer and Q. Sun, Helmholtz equation and non-singular boundary elements applied to multi-disciplinary physical problems, Commun. Theor. Phys. **74**, 085003 (2022).